High-End Manufacturing
https://www.sciltp.com/journals/hem



Article

A Fuzzy Sliding Mode-Based Hybrid Control Algorithm for Air-Bearing Machining Systems

Xinyi Wang, Zhen Tong *, Zheng Gong and Dongze Wang

School of Mechanical Engineering, Shanghai Jiao Tong University, Shanghai 200240, China
* Correspondence: z.tong@sjtu.edu.cn

How To Cite: Wang, X.; Tong, Z.; Gong, Z.; et al. A Fuzzy Sliding Mode-Based Hybrid Control Algorithm for Air-Bearing Machining Systems. *High-End Manufacturing* **2026**, *1*(1), 1.

Received: 10 September 2026
Revised: 15 October 2026
Accepted: 20 October 2026
Published: 2 November 2026

Abstract: Air-bearing systems are extensively applied in ultra-precision machining owing to their non-contact operation and nanometer-scale positioning accuracy. However, the compressibility of the air film and inherent low damping compromise system stability under dynamic disturbances. To address these challenges, this paper presents a fuzzy sliding mode-based hybrid control algorithm. The architecture integrates proportional-integral-derivative (PID) control, velocity/acceleration feedforward (FF), and fuzzy sliding mode control (FSMC), where fuzzy logic is employed to suppress sliding mode chattering. Simulations and experiments were performed on low- and high-frequency testbeds. The air-bearing testbed achieved a rise time of 8 ms and an overshoot of 0.29%, while the FTS system achieved a rise time of 1 ms and an overshoot of 3.08%. The measured closed-loop −3 dB bandwidth of the FTS system was approximately 500 Hz. In micro-pit machining, the arithmetic mean surface height Sa decreased from 10.4 nm with PID-FF to 7.1 nm with PID-FF-FSMC, corresponding to a reduction of 31.73%.

Keywords: air-bearing; fast tool servo; hybrid control algorithm; fuzzy sliding mode control

1. Introduction

Air-bearings are fundamental components for ultra-precision motion guidance, widely used in aerospace, medical devices, semiconductor lithography, and laser machining [1–4]. Owing to the non-contact operation and environmental friendliness, air bearings have emerged as a promising solution for the ultra-precision spindle [5], positioning stages [6], and fast tool servo (FTS) nanometric cutting systems [7]. However, their inherent high compressibility of air induces pressure-response hysteresis, rendering air-bearing systems highly sensitive to high-frequency disturbances and rapid servo movements [8]. Although structural optimization, such as bio-inspired compound restrictor [9] and Laval-nozzle-inspired outlet structure [10], demonstrates helpfulness for the support performance, such improvements do not directly compensate for trajectory-dependent lag, time-varying cutting forces, and machining vibrations. Consequently, advanced motion control strategies are imperative for air-bearing-based FTS machining systems [11].

To mitigate the effects of external disturbances, FTS control systems have evolved from traditional linear control schemes, including proportional-integral-derivative (PID) [12], feedforward [13], feedback [14], and repetitive control [15], toward advanced nonlinear algorithms. Derived from PID control, active disturbance rejection control (ADRC) employs state observers to compensate for dynamic nonlinearities [16], but its practical application is often constrained by a reliance on accurate system modeling and complex parameter tuning [17]. A Q-learning algorithm was thereby developed for the adaptive online joint tuning of ADRC in a simulated FTS system [18], attaining a maximum tracking error of 18.91 μm for a 5 mm, 100 Hz sinusoidal trajectory. Meanwhile, sliding mode control (SMC) has been widely favored for its robust performance and disturbance compensation. Nevertheless, the discontinuous control law in SMC induces potential chattering and excites unmodeled high-

Copyright: © 2026 by the authors. This is an open access article under the terms and conditions of the Creative Commons Attribution (CC BY) license (https://creativecommons.org/licenses/by/4.0/).
Publisher's Note: Scilight stays neutral with regard to jurisdictional claims in published maps and institutional affiliations.

frequency dynamics, which is particularly detrimental to low-damping air-bearing systems. Higher-order sliding mode control (HOSMC), including the super-twisting algorithm, has been proposed to alleviate chattering by shifting the discontinuity to higher-order derivatives of the sliding variable [19,20]. However, some practical implementations require derivative estimation or auxiliary observers. In high-bandwidth FTS systems, such estimation increases sensitivity to measurement noise and unmodeled structural resonances [21], which may induce severe phase lags challenge during high-frequency tracking [22].

Given the inherent limitations of linear and nonlinear control algorithms, considerable efforts have been devoted to developing hybrid strategies that exploit complementary advantages [23]. Meng et al. [24] combined a dual-loop controller, disturbance observer, and real-time iterative compensation module for FTS systems. The root mean square (RMS) error was reduced to below 0.1% under trajectory variations and external disturbances. To further improve manufacturing accuracy, a hybrid control scheme integrating robust feedback, adaptive feedforward, and online trajectory compensation was proposed. Experiments on an air-bearing nano-motion stage reported a contouring accuracy of 7 nm over 100 mm strokes and an error fluctuation of 4.13 nm under a 3.8 kg payload and external disturbances [25]. More recently, intelligent control strategies, such as fuzzy logic [26] and neural networks [27,28], have attracted increasing attention in the hybrid architecture owing to the promising disturbance rejection capabilities. To smooth the discontinuous control laws, fuzzy control was incorporated into the fractional-order SMC for permanent magnet linear motors. The mean absolute error was reduced from 52.96% (PID) to 19.32% (AFFSMC) under an 8 kg payload, indicating superior robustness against parameter variations and external disturbances [29].

Overall, nonlinear control strategies and intelligent algorithms have been widely applied to address the susceptibility limitation of air-bearings. A previous study [30] developed a hybrid control algorithm to effectively reduce phase error and overshoot in FTS systems, but the chattering in SMC remains a bottleneck limiting system control accuracy. In this study, a fuzzy sliding mode-based hybrid control algorithm is developed for air-bearing machining systems. The hybrid control system consists of PID, velocity/acceleration feedforward (FF), and fuzzy sliding mode control (FSMC). The FF module effectively compensates for system inertia and phase lag, while the FSMC contributes to overshoot suppression and disturbance rejection. Modeling, simulations, and comparative experiments are performed on both air-bearing and FTS testbeds to evaluate the proposed control strategy. Finally, micro-pit FTS machining experiments are conducted to further validate the robustness, adaptability, and practical applicability of the algorithm.

2. System Modeling and Algorithm Development

2.1. Control System Modeling

Figure 1a illustrates the architecture of the in-house-developed air-bearing systems. A multi-axis precision motion controller CK3M (Omron, Kyoto, Japan) is employed to generate the driving voltage signal for the open-loop subsystem, which consists of the motor drive, linear motor, air-bearing guideway, and mechanism. The position signal is measured by an optical encoder (Renishaw, Wotton-under-Edge, UK) and fed back to the controller, where the control algorithms are implemented to achieve closed-loop position control.

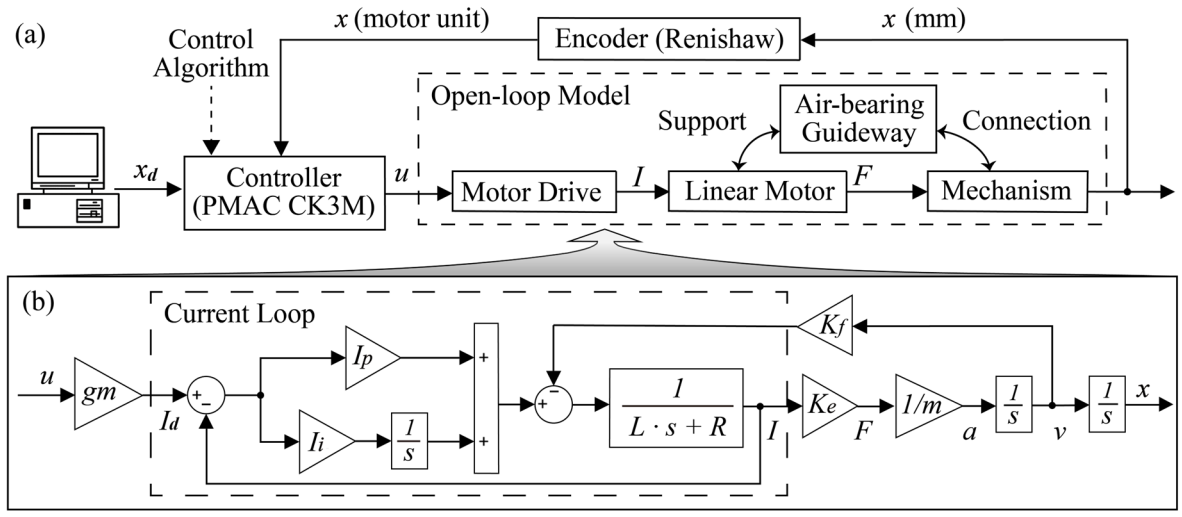


Figure 1. System architecture. (**a**) System framework; (**b**) Open-loop model.

The open-loop simulation model is depicted in Figure 1b, and its corresponding transfer function is given by Equation (1). A linear motor driver with 5 kHz bandwidth functions as a PI controller for current loop tuning.

$$G(s)=\frac{X(s)}{U(s)}=\frac{K_f}{mLs^3+mRs^2+K_fK_e\cdot s} \tag{1}$$

where m is the moving mass, L is the inductance, R is the resistance, K_f is the force constant, and K_e is the back EMF constant. Specific parameters for the air-bearing and FTS systems are listed in Table 1.

Table 1. Parameters of the air-bearing system and FTS system.

Parameters	Air-Bearing System	Fast Tool Servo System	Unit
gm	0.8	0.6	A/V
I_p	53.33	31.11	-
I_i	13,111.11	10,444.44	-
R	5.9	4.7	Ω
L	2.4	1.4	mH
K_f	21.8	22.7	N/A
K_e	25.2	18.6	V/(m·s^{-1})
m	35	3.4	kg

2.2. Control Algorithm Development

This study proposes a hybrid control algorithm, integrating PID, FF, and FSMC to optimize system performance. The resulting control architecture is illustrated in the block diagram in Figure 2. A zero-order hold is employed to maintain the discrete command until the next sampling instant, producing the piecewise-constant input applied to the state-space model:

$$u_{model}(t)=u[k],\ kT_s\le t<(k+1)T_s \tag{2}$$

where u_{model} is the input to the state-space model, and the sampling interval T_s = 0.000125 s corresponds to the PMAC servo frequency of 8 kHz.

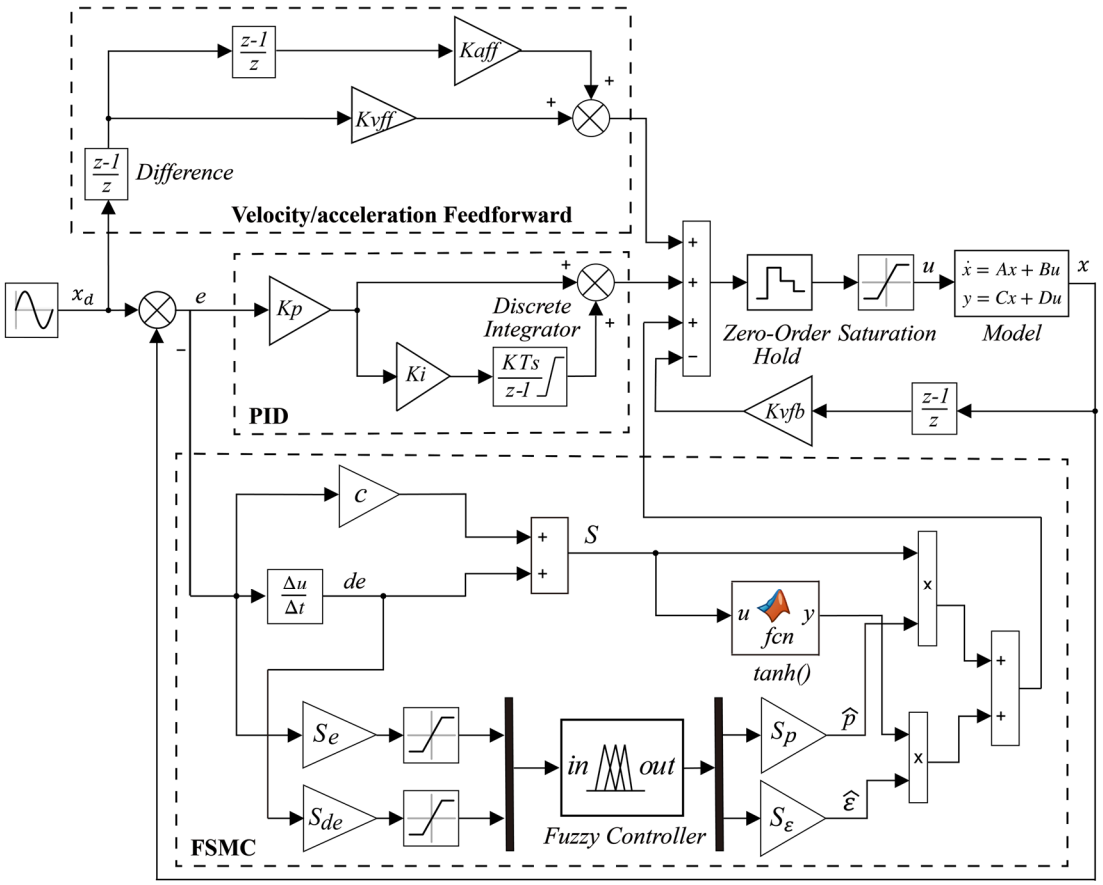


Figure 2. Control block diagram of the hybrid algorithm.

Based on traditional PID, FF is introduced to compensate for inertia lag and enhance dynamic response by incorporating the reference velocity and acceleration into the control law. For SMC, the linear sliding surface (Equation (8)) yields exponential decay of the tracking error when $S = 0$. Motivated by the exponential reaching law, the control output of FSMC is designed to combine linear and nonlinear terms (Equation (7)), with an adaptive fuzzy logic integrated to tune the damping coefficient $\hat{\varepsilon}$ and stiffness coefficient $\hat{p}$ online. The overall control output is the sum of the three control components, with formulations as detailed:

$$u[k] = u[k]_{\text{PID}} + u[k]_{\text{FF}} + u[k]_{\text{FSMC}} \tag{3}$$

$$u[k]_{\text{PID}} = K_p e[k] + K_i \sum_{i=1}^{k} e[i] - K_{vfb}\left(x[k] - x[k-1]\right) \tag{4}$$

$$u[k]_{\text{FF}} = K_{vff}\left(x_d[k] - x_d[k-1]\right) + K_{aff}\left(v_d[k] - v_d[k-1]\right) \tag{5}$$

$$e[k] = x_d[k] - x[k],\ v[k] = \frac{x[k] - x[k-1]}{T_s},\ v_d[k] = \frac{x_d[k] - x_d[k-1]}{T_s} \tag{6}$$

$$u[k]_{\text{FSMC}} = \hat{\varepsilon} \cdot f(S) + \hat{p}S, \varepsilon > 0, \text{p} > 0 \tag{7}$$

$$S = ce + \dot{e},\ \dot{e}[k] = \frac{e[k] - e[k-1]}{T_s} \tag{8}$$

$$f(S) = \tanh\left(\frac{\varphi S}{2}\right) = \frac{1 - e^{-\varphi S}}{1 + e^{-\varphi S}} \tag{9}$$

where $u[k]_{\text{PID}}$, $u[k]_{\text{FF}}$, and $u[k]_{\text{FSMC}}$ are the control laws of the PID, FF, and FSMC components, respectively. K_p and K_i are the proportional and integral gains, while K_{vfb}, K_{vff}, and K_{aff} are the velocity feedback, velocity feedforward, and acceleration feedforward gains, respectively. v_d is the command velocity, and c is the coefficient of the sliding surface. The tracking error is defined as the difference between the command displacement x_d and actual displacement x, while the velocity and error-derivative signals are derived algebraically from the sampled displacement signals using discrete-time differentiation. Furthermore, a smooth approximation $f(S)$ in Equation (9) is used to replace the discontinuous sign function, with a constant $\varphi = -1 \times 10^{-8}$ applied in this study.

To reduce chattering, the fuzzy logic is designed to adaptively tune the sliding mode coefficients based on real-time state variables. Specifically, the error e and its derivative ė were input to characterize the system state relative to the sliding surface. Large absolute values of e and ė indicate that the system state is far from the sliding surface (Equation (8)). Accordingly, the fuzzy controller increases the positive coefficients p and ε to enlarge the control output $|u|$ further, accelerating the system's convergence toward the sliding surface [31,32]. As e and $\dot{e}$ approach zero, the values of p and ε are adaptively reduced to slow the sliding motion, suppress chattering, and improve steady-state performance. The fuzzy rule and surface are detailed in Table 2 and Figure 3, respectively.

Table 2. Fuzzy rule table for FSMC.

e \ $\dot{e}$	NB	NM	NS	Z	PS	PM	PB
NB	PB	PB	PB	PB	PM	PS	Z
NM	PB	PB	PB	PM	PS	Z	PS
NS	PB	PB	PM	PS	Z	PS	PM
Z	PB	PM	PS	Z	PS	PM	PB
PS	PM	PS	Z	PS	PM	PB	PB
PM	PS	Z	PS	PM	PB	PB	PB
PB	Z	PS	PM	PB	PB	PB	PB

NB = Negative Big; NM = Negative Medium; NS = Negative Small; Z = Zero; PS = Positive Small; PM = Positive Medium; PB = Positive Big.

The input variables e and $\dot{e}$ are normalized to the range of [−1, 1] using scaling factors s_e and s_{de}, respectively. These inputs are mapped to seven fuzzy subsets {NB, NM, NS, Z, PS, PM, PB}, and the outputs are fuzzified over

the interval [0, 1] with subsets {Z, PS, PM, PB}. The same normalized fuzzy output is rescaled separately using factors S_p and S_ε to obtain p and ε, respectively. Triangular membership functions of the fuzzy logic are described in Figure 4.

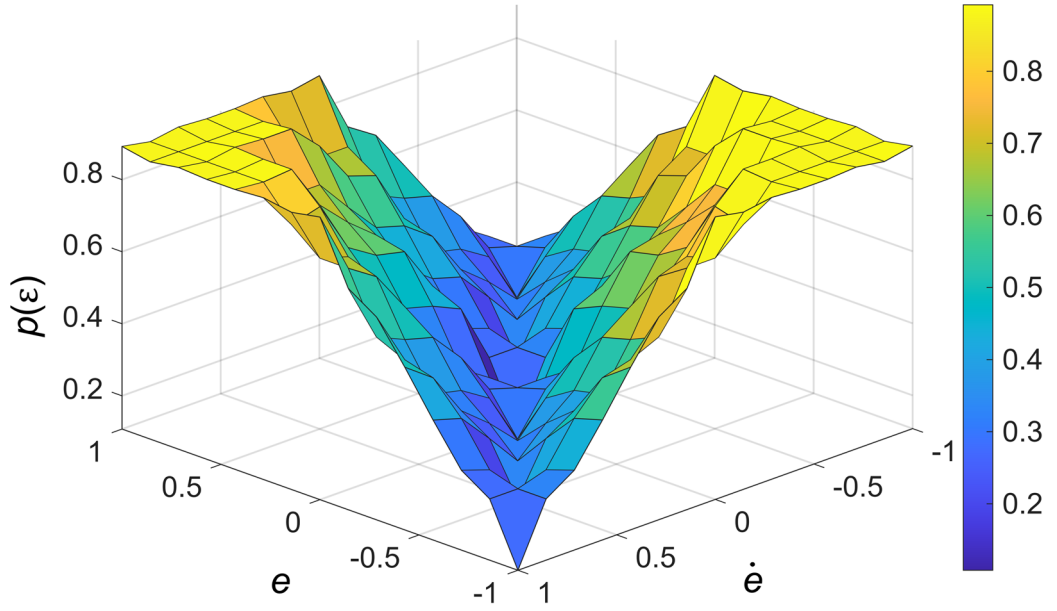


Figure 3. Fuzzy rule surface of FSMC. The two horizontal axes are input parameters e and $\dot{e}$, and the vertical axis represents output parameters p and ε.

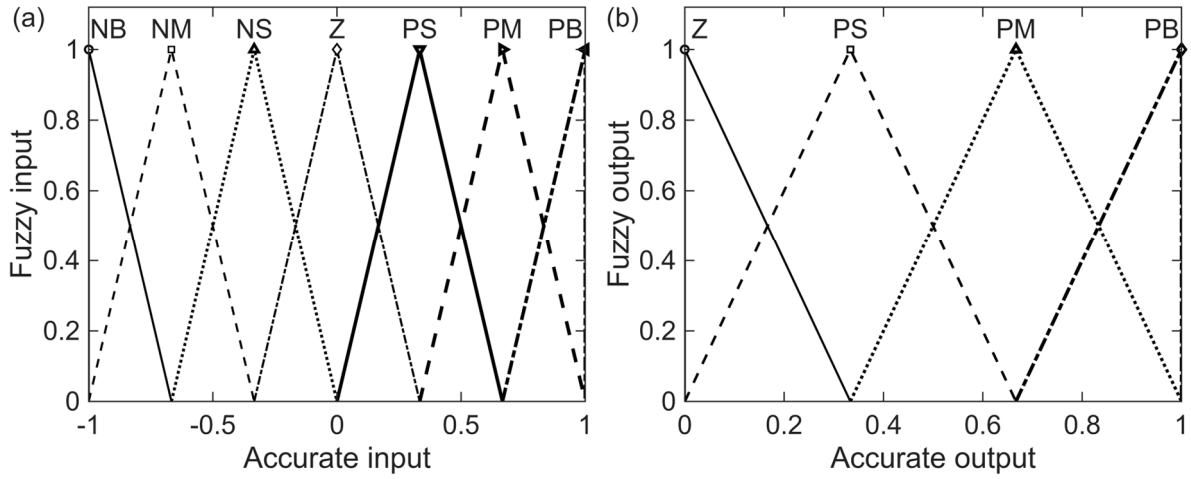


Figure 4. Membership functions. (**a**) Fuzzy input; (**b**) Fuzzy output. Centroid defuzzification methods are adopted, with fuzzy subsets uniformly distributed within fuzzy domains.

To evaluate the efficacy of the proposed fuzzy logic, both step response and sinusoidal tracking simulations were conducted. The 0.1 mm step response (Figure 5a) indicates that the incorporation of fuzzy logic noticeably enhances dynamic response and suppresses the chattering observed in PID-FF-SMC. As shown in Figure 5b, the severe control output chattering under PID-FF-SMC is significantly alleviated by the online adaptive tuning of fuzzy control. To further assess system robustness, a sinusoidal disturbance was applied to emulate periodic cutting forces encountered during actual machining processes:

$$f_{\sin} = A_1 \sin(2\pi ft) + A_2 \sin(4\pi ft) \tag{10}$$

where $f_{\sin}$ is the disturbance signal, A_1 and A_2 are disturbance amplitudes, and f is the sine frequency.

As illustrated in Figure 5c,d, the tracking error increased from 5.98% to 8.56% for PID-FF-SMC, and from 2.64% to 3.21% for PID-FF-FSMC under the applied disturbance. The corresponding increases were 2.58 and 0.57 percentage points, respectively. These results indicate a smaller disturbance-induced increase in tracking error for PID-FF-FSMC under the tested conditions. The control-output comparison in Figure 5b also shows smaller oscillations for PID-FF-FSMC than for PID-FF-SMC.

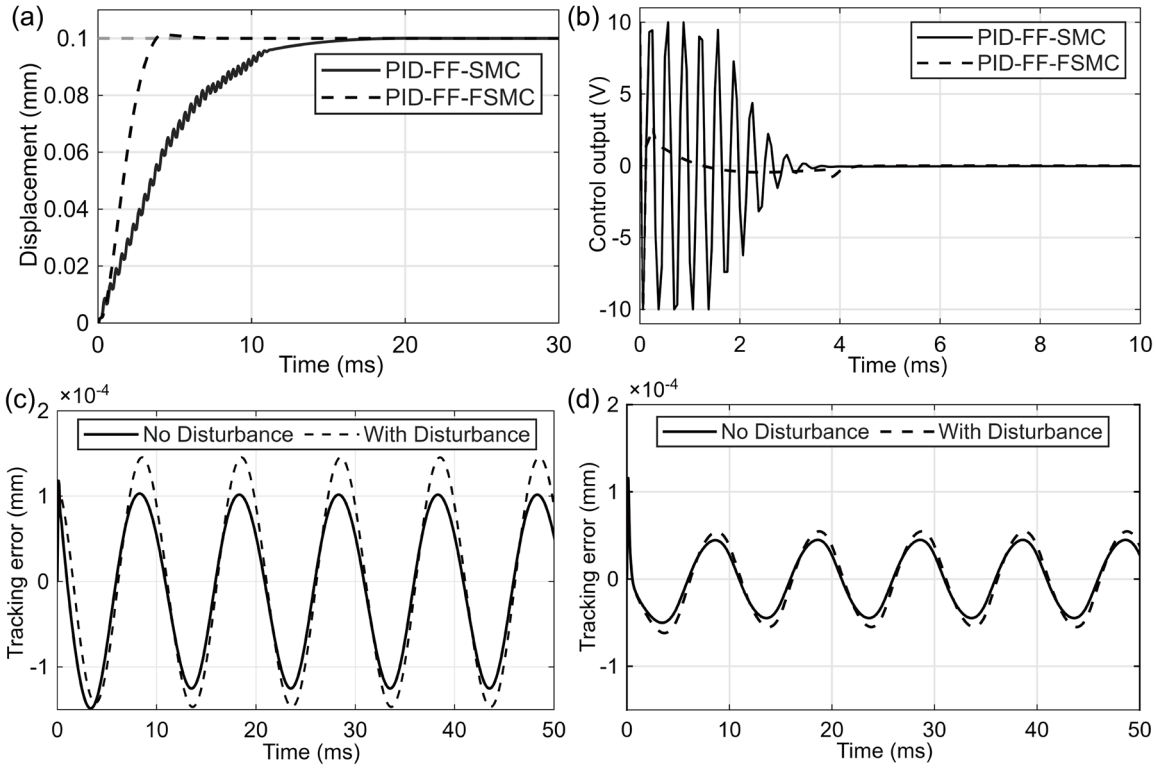


Figure 5. Simulation performance of fuzzy control. (**a**) 0.1 mm step response; (**b**) 0.1 mm step control output; (**c**) Tracking error of PID-FF-SMC (1.7 μm at 100 Hz); (**d**) Tracking error of PID-FF-FSMC (1.7 μm at 100 Hz).

2.3. Simulation of Control System Performance

To evaluate the system performance, system identification was first conducted to establish the simulation model. The high-frequency FTS system was excited in open loop using a swept-sine voltage signal, with the input and measured displacement response shown in Figure 6. A second-order state-space model (Equation (11)) was identified from the input–output data using the MATLAB (R2025b) System Identification Toolbox.

$$\begin{cases} \dot{x}(t) = \begin{bmatrix} 1 & -2.87e^{-4} \\ 2.44e^{-4} & 1 \end{bmatrix} x(t) + \begin{bmatrix} 9.54e^{-12} \\ 3.27e^{-8} \end{bmatrix} u(t) \\ y(t) = \begin{bmatrix} -7.11e^{11} & -5.12e^{7} \end{bmatrix} x(t) \end{cases} \tag{11}$$

where $x(t)$ is the state vector, $u(t)$ is the input, and $y(t)$ is the output.

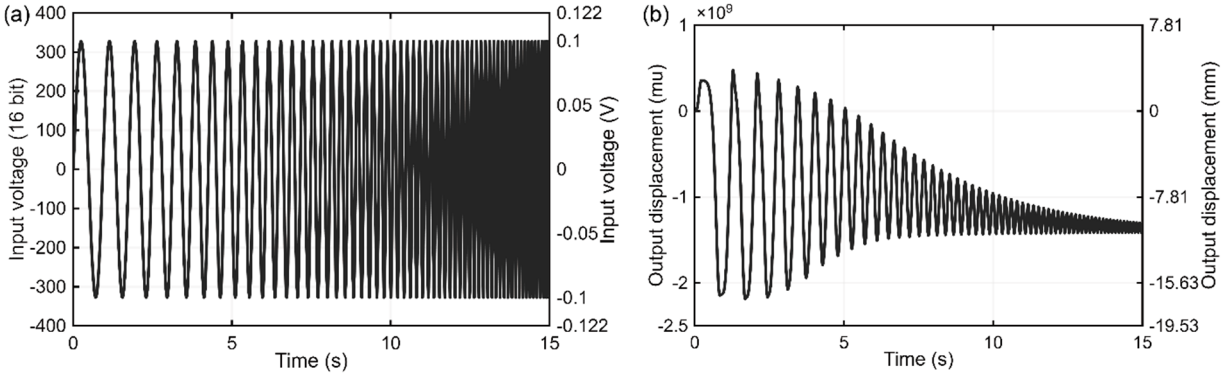


Figure 6. Open-loop frequency response. (**a**) Swept-sine input: a sine voltage signal with 0.1 V amplitude and linearly increasing frequency (1–100 Hz); (**b**) Frequency-sweep output.

The performance of four different control algorithms was tested, including PID, PID-FF, FSMC, and the proposed hybrid PID-FF-FSMC. As demonstrated in Figure 7a and Table 3, for the simulated 1 mm step input, PID-FF-FSMC achieved a rise time of 2.56 ms and an overshoot of 0.13%. Its rise time was approximately 66.1% shorter than the 7.56 ms obtained with FSMC, while its overshoot was lower than the 0.45% obtained with FSMC.

Compared with PID and PID-FF, whose rise times were both 2 ms, the hybrid controller had a longer rise time but lower overshoot (6.44% and 6.43% for PID and PID-FF, respectively).

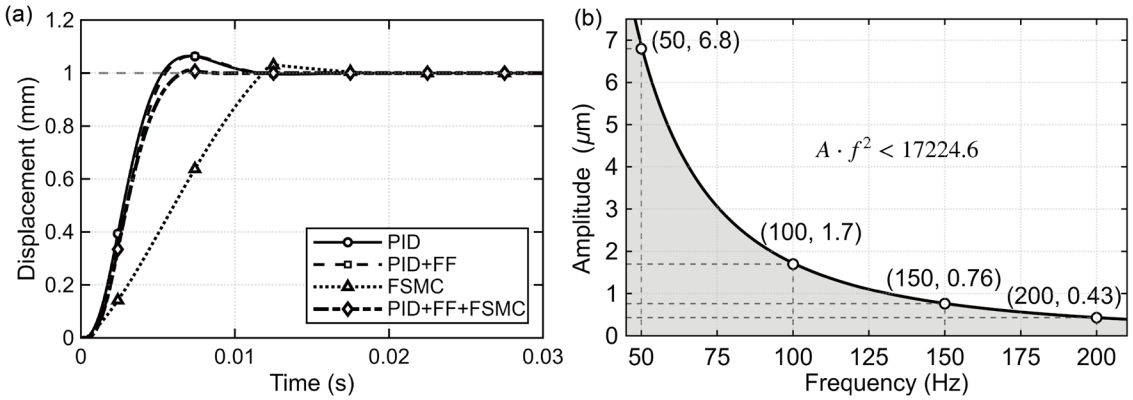


Figure 7. (**a**) Step response of four control algorithms; (**b**) Amplitude-frequency of input sine signals.

Table 3. Step performance metrics of four control algorithms.

Control Algorithms	Rise Time (ms)	Overshoot
PID	2	6.44%
PID-FF	2	6.43%
FSMC	7.56	0.45%
PID-FF-FSMC	2.56	0.13%

For sinusoidal tracking tests, the input sine signals were selected in accordance with the linear motor. The sine motion can be expressed as Equations (12)–(14).

$$x(t) = A\sin(\omega t) \tag{12}$$

$$a(t) = \ddot{x}(t) = -A\omega^2 sin(\omega t) \tag{13}$$

$$F(t) = ma = -mA\omega^2\sin(\omega t) \tag{14}$$

The RMS force of the system can be further calculated as in Equation (15). Based on the continuous thrust of the motor, the corresponding amplitude-frequency curve (Equation (16)) of input sinusoidal signals is plotted in Figure 7b. Four representative sine signals, including 6.8 μm at 50 Hz, 1.7 μm at 100 Hz, 0.76 μm at 150 Hz, and 0.43 μm at 200 Hz, were selected to evaluate the system's limiting performance. In the following discussion, the 1.7 μm at 100 Hz sinusoidal signal is taken as a representative case for evaluating sinusoidal tracking performance of control algorithms.

$$F_{RMS} = \sqrt{\frac{1}{T}\int_0^T [F(t)]^2 dt} = \frac{\sqrt{2}}{2} \cdot F_{pk} \le \frac{\sqrt{2}}{2} mA\omega^2 \tag{15}$$

$$A \cdot f^2 < 17224.6 \tag{16}$$

The main performance metrics, including root-mean-square error (*RMSE*), steady-state error (*SSE*), amplitude difference (*AD*), and phase difference (*PD*), are determined from Equations (17)–(20). The *SSE* is calculated after the first period (Equation (18)).

$$RMSE = \frac{\sqrt{\frac{1}{N}\sum_{k=1}^{N}\left(x_d[k] - x[k]\right)^2}}{A} \tag{17}$$

$$SSE = \frac{max\,|\,x_d[k] - x[k]\,|}{A}, kT_s > 1/f \tag{18}$$

$$AD = \frac{A - \max(|x|)}{A} \tag{19}$$

$$PD = \frac{t_{d,p} - t_p}{T} \times 360° \tag{20}$$

where $t_{d,p}$ and t_p are the peak time of command and actual displacement, respectively.

A comprehensive comparison of tracking performances is presented in Figure 8. For the simulated 1.7 μm, 100 Hz trajectory, PID-FF-FSMC achieved an *RMSE* of 1.05% and an *SSE* of approximately 1.235%, compared with 2.832% and 3.957% for PID-FF. The amplitude difference was 1.095%, and the peak-based phase estimate was 0° for this test. These results show lower tracking errors than the comparison controllers under the specified simulation conditions.

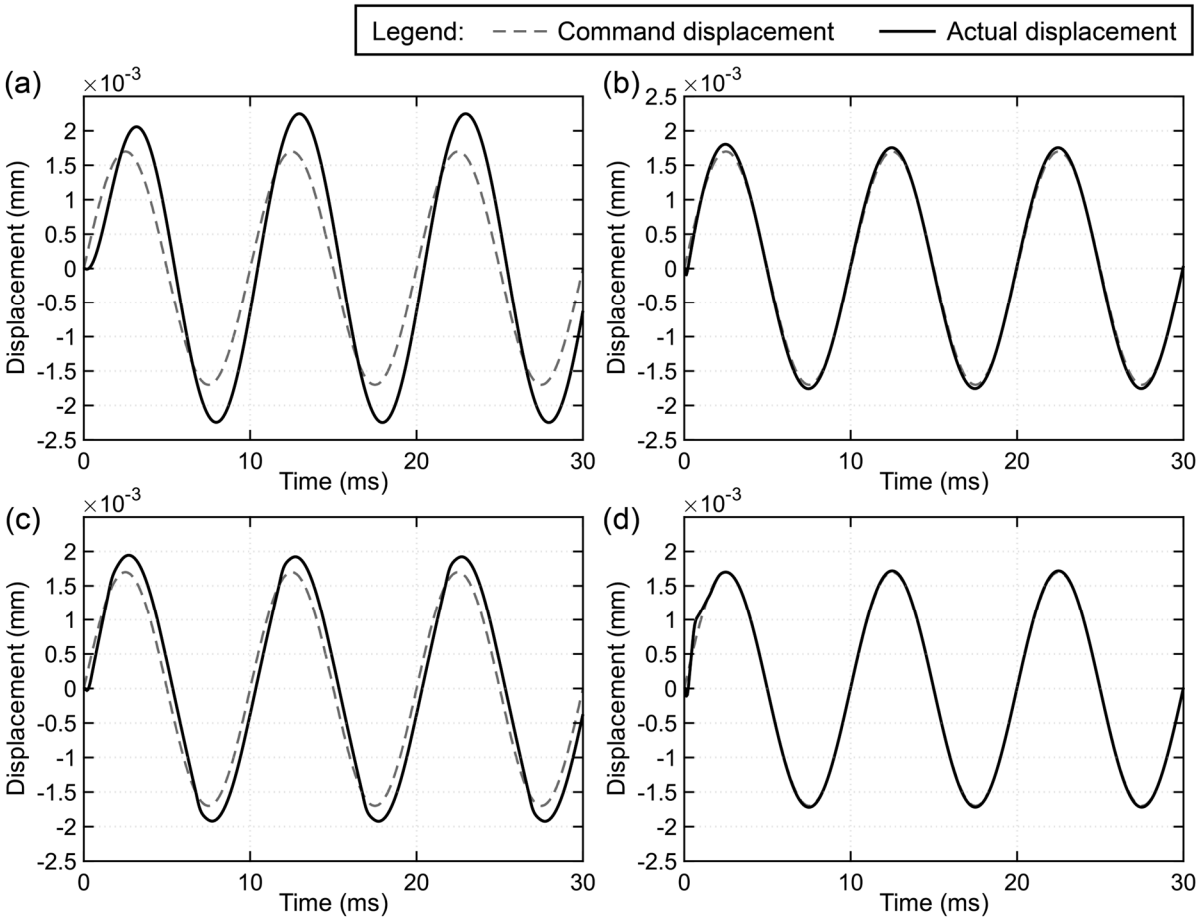


Figure 8. Simulation tracking performance of different algorithms (1.7 μm at 100 Hz) under (**a**) PID; (**b**) PID-FF; (**c**) FSMC; (**d**) PID-FF-FSMC.

Among the performance metrics, steady-state error (*SSE*) is the most critical, as the fundamental goal of control algorithms is to maintain *SSE* within an acceptable bound. The sinusoidal tracking error under 1.7 μm at 100 Hz is depicted in Figure 9. Sine responses under all control algorithms converge to a steady state after a period, with PID-FF-FSMC exhibiting the minimal tracking error. The simulated *SSE* results are summarized in Table 4. PID control suffers from severe degradation as frequency increases, with tracking error soaring from 11.708% at 50 Hz to over 113% at 200 Hz, due to limited bandwidth and inertia-induced phase lag. PID-FF markedly improves tracking performance at low and mid-range frequencies through predictive compensation, but its effectiveness diminishes at higher frequencies. In contrast, the PID-FF-FSMC demonstrated the lowest *SSE* among the four tested controllers at each simulated frequency. At 200 Hz and a command amplitude of 0.43 μm, its *SSE* was 7.316%, compared with 26.648% for PID-FF.

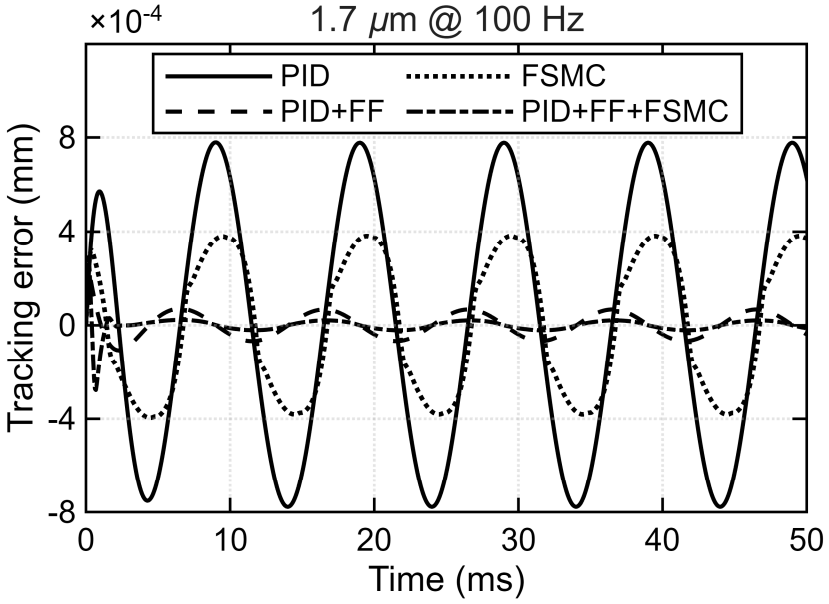


Figure 9. Simulation tracking errors of different algorithms (1.7 μm at 100 Hz).

Table 4. Steady-state error of sinusoidal tracking simulations.

Control Algorithms	6.8 μm at 50 Hz	1.7 μm at 100 Hz	0.76 μm at 150 Hz	0.43 μm at 200 Hz
PID	11.708%	45.750%	87.247%	113.140%
PID-FF	0.228%	3.957%	14.362%	26.648%
FSMC	8.510%	22.433%	37.603%	53.221%
PID-FF-FSMC	0.134%	1.2352%	3.567%	7.316%

3. Experimental Evaluation of Dynamic Performance

3.1. Air-Bearing Test

Two experimental platforms were used to evaluate the controller structure under different motion conditions. In the initial experiment, the air-bearing guideway was configured for low-frequency operation. The system was actuated by the TA310 driver (Trust Automation, San Luis Obispo, CA, USA) and I_FORCE 210 linear motor (Parker, Cleveland, OH, USA). The physical setup is depicted in Figure 10a, with detailed control parameters listed in Table 5.

Table 5. Control parameters of the low-frequency air-bearing system.

Parameters	Value	Parameters	Value
K_p	0.45	c	120
K_i	0.001	S_e	0.2
K_{vff}	15	S_{de}	2×10^{-4}
K_{aff}	273	S_p	0.08
K_{vfb}	15	S_ε	50

The 0.1 mm step response reveals rapid transient dynamics with pronounced overshoot under PID and PID-FF. In contrast, the FSMC and hybrid control exhibit smoother settling characteristics (Figure 10b). The corresponding metrics are summarized in Table 6. Both PID and PID-FF achieve comparable rise times (6.13 ms) with drastic overshoot (14.5%). FSMC suppresses the overshoot to 2.66%, but at the cost of a nearly doubled rise time (11.5 ms). In contrast, the proposed PID-FF-FSMC rises rapidly (8 ms) and stabilizes after reaching the command position with near-zero overshoot (0.29%), thereby enabling a compromise between rise time and overshoot.

Table 6. Step response results of four control algorithms.

Control Algorithms	Rise Time (ms)	Overshoot
PID	6.13	14.55%
PID-FF	6.13	14.53%
FSMC	11.5	2.66%
PID-FF-FSMC	8	0.29%

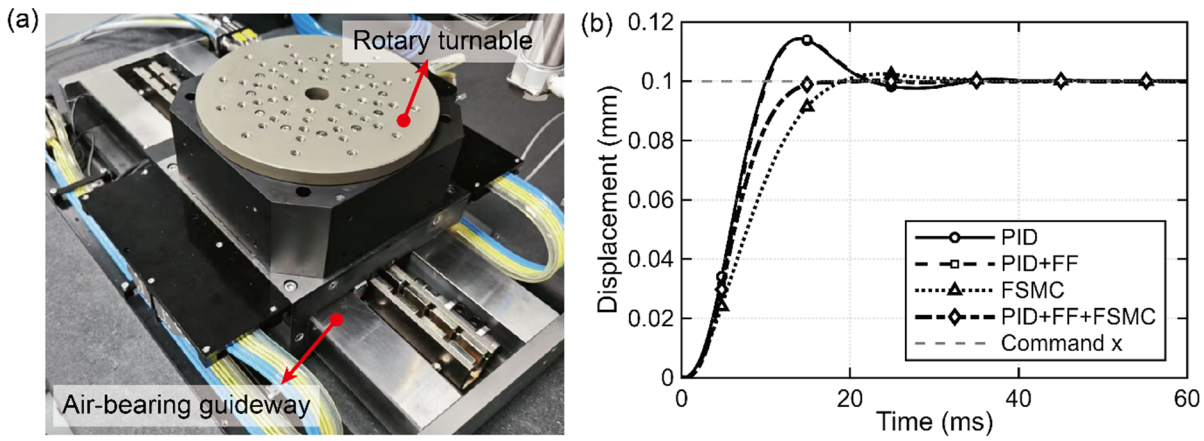


Figure 10. (**a**) Physical setup of the air-bearing system; (**b**) Step response of four control algorithms (0.1 mm).

A sine signal of 0.1 mm at 10 Hz is input to execute the tracking test, and the performance and metrics are shown in Figure 11 and Table 7, respectively. The hybrid control algorithm accomplishes an *RMSE* of 1.077% and an *SSE* of 1.010%, compared with 2.118% and 2.249% for PID-FF, demonstrating a remarkable improvement over PID and FSMC. Regarding the dynamic characteristics, PID-FF-FSMC exhibited a phase difference of 0.400° and an amplitude difference of 0.630%, markedly eliminating phase distortion as shown in Figure 11a. Furthermore, a slight phase lag (<2°) is observed in all algorithms, with a negligible effect on the overall tracking accuracy. These results demonstrate the excellent tracking performance of the proposed hybrid algorithm, enabling high-precision and stable positional control in low-frequency air-bearing systems.

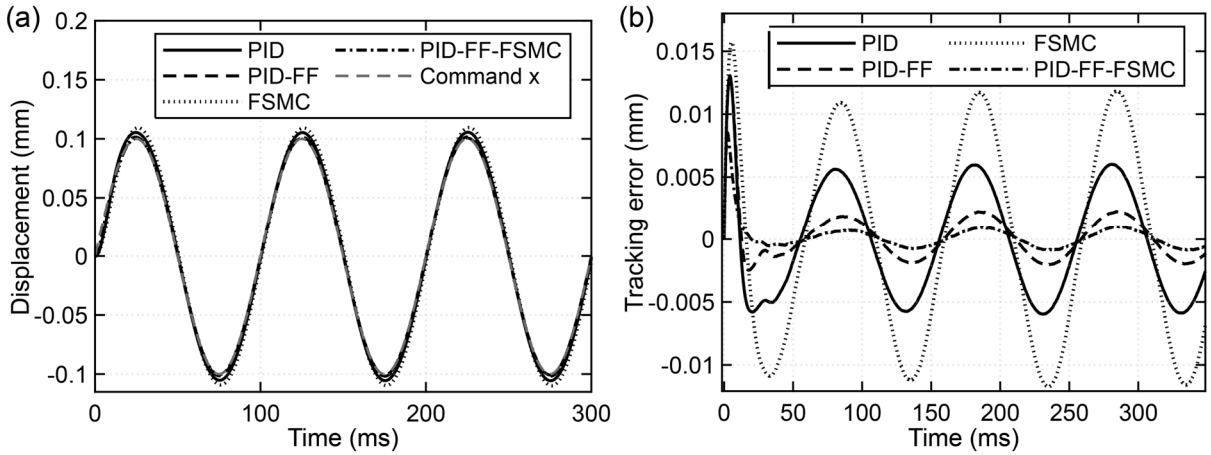


Figure 11. Sine response of different algorithms under 0.1 mm at 10 Hz. (**a**) Tracking response; (**b**) Tracking error.

Table 7. Sine tracking performance metrics under 0.1 mm at 10 Hz.

Control Algorithms	*RMSE*	*SSE*	*AD*	*PD*
PID	4.412%	6.020%	5.545%	0.601°
PID-FF	2.118%	2.249%	1.669%	0.400°
FSMC	8.166%	11.830%	9.586%	1.800°
PID-FF-FSMC	1.077%	1.010%	0.630%	0.400°

3.2. Fast Tool Servo Test

The experimental setup of the high-frequency FTS system is illustrated in Figure 12a. The TA330 motor drive (Trust Automation, San Luis Obispo, CA, USA) and T1-3B linear motor (Parker, Cleveland, OH, USA) were employed for high-frequency operation, with control parameters listed in Table 8. The step response performance and the corresponding metrics for the four control algorithms are presented in Figure 12b and Table 9, respectively.

According to Figure 12b, PID-FF-FSMC achieved a rise time of 1 ms and an overshoot of 3.08%. Compared with PID-FF, its rise time increased from 0.75 ms to 1 ms, while the overshoot decreased from 6.49% to 3.08%. Compared with FSMC, it had a shorter rise time and lower overshoot. These measurements describe the transient-response compromise achieved on the FTS platform.

Table 8. Control parameters of the high-frequency FTS system.

Parameters	Value	Parameters	Value
K_p	0.0005	c	200
K_i	0.001	S_e	4×10^{-4}
K_{vff}	0.011	S_{de}	3×10^{-7}
K_{aff}	0.15	S_p	2×10^{-6}
K_{vfb}	0.011	S_ε	70

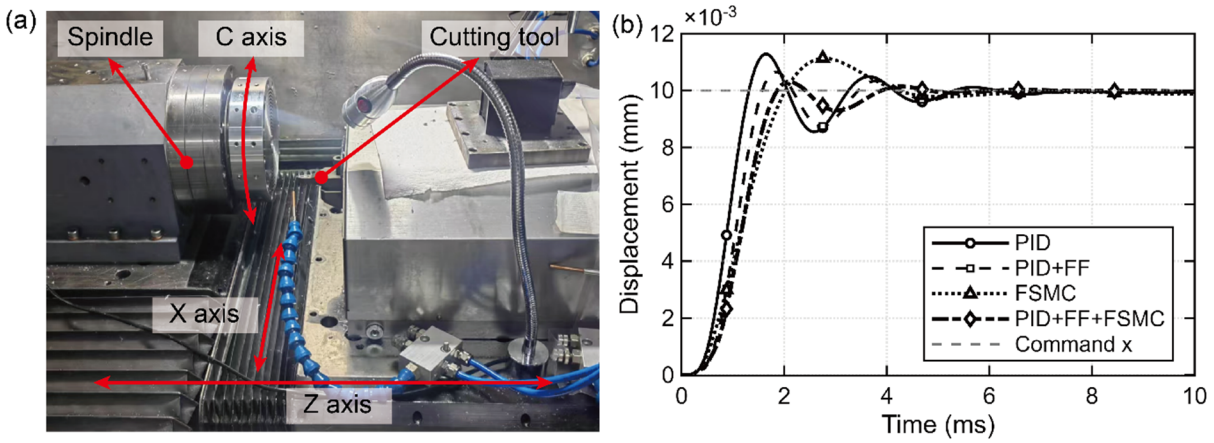


Figure 12. (**a**) Physical setup of the FTS system; (**b**) Step response of four control algorithms (0.01 mm).

Table 9. Step response performance of different algorithms (0.01 mm).

Control Algorithms	Rise Time (ms)	Overshoot
PID	0.69	12.85%
PID-FF	0.75	6.49%
FSMC	1.25	11.28%
PID-FF-FSMC	1	3.08%

For sinusoidal tracking, the same four signals marked in Figure 7b were employed as input. The tracking response under 1.7 μm at 100 Hz is plotted in Figure 13a. All four control algorithms exhibit error peaks within the first quarter-cycle before converging to a steady-state within one period, with PID and FSMC demonstrating noticeable phase lag (Figure 13b). The *SSE* of the hybrid control algorithm is 4.31%, which outperforms the PID-FF controller (6.8%) by 36.6% and exhibits markedly superior efficiency compared to the standalone PID and FSMC strategies. For this representative case, the hybrid controller achieves an amplitude difference (*AD*) of 3.356% and a phase difference (*PD*) of 2.25°. A comprehensive evaluation of sinusoidal tracking errors across tested frequencies is summarized in Table 10.

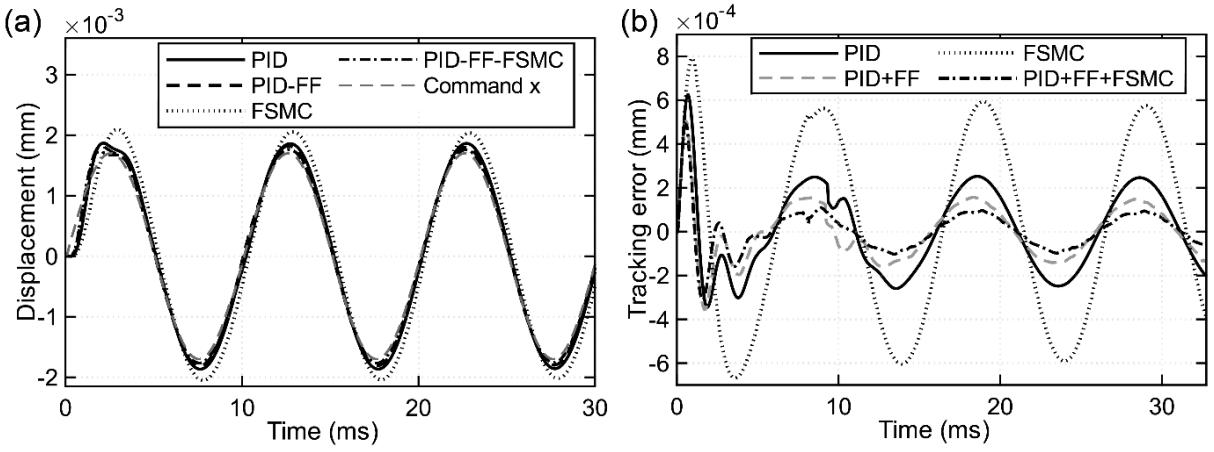


Figure 13. Sine response of different algorithms under 1.7 μm at 100 Hz. (**a**) Tracking response; (**b**) Tracking error.

Table 10. Sinusoidal tracking error of different algorithms.

Control Algorithms	6.8 μm at 50 Hz	1.7 μm at 100 Hz	0.76 μm at 150 Hz	0.43 μm at 200 Hz
PID	2.49%	11.31%	30.95%	47.71%
PID-FF	1.85%	6.80%	16.35%	31.55%
FSMC	5.83%	27.25%	72.56%	111.31%
PID-FF-FSMC	1.31%	4.31%	10.39%	17.26%

PID-FF-FSMC produced the lowest steady-state tracking error among the four tested controllers at each of the four experimental frequencies, followed by PID-FF, PID, and FSMC in descending order of tracking precision. Although FSMC substantially suppresses overshoot, its inherently sluggish dynamic response leads to significant performance deterioration as frequency rises. Notably, the hybrid control algorithm achieves a tracking error of 17.26% with 0.43 μm at 200 Hz, in contrast to 47.71% for the PID control algorithm. The poor performance of PID at 200 Hz is primarily attributed to severe phase lag and limited robustness to nonlinear disturbances. These findings highlight the benefits of the hybrid control algorithm. The FF compensation significantly alleviates phase lag, while FSMC reduces overshoot and suppresses uncertain vibrations. The synergistic architecture makes the algorithm well-suited for high-frequency applications.

To quantify the FTS dynamics, a closed-loop frequency-response test was conducted. Excitation frequency and output displacement were recorded to construct the Bode diagram (Figure 14). The magnitude curve depicts a −3 dB attenuation point at 500 Hz, indicating that the proposed algorithm can maintain high loop gain and strong disturbance rejection across a broad frequency range.

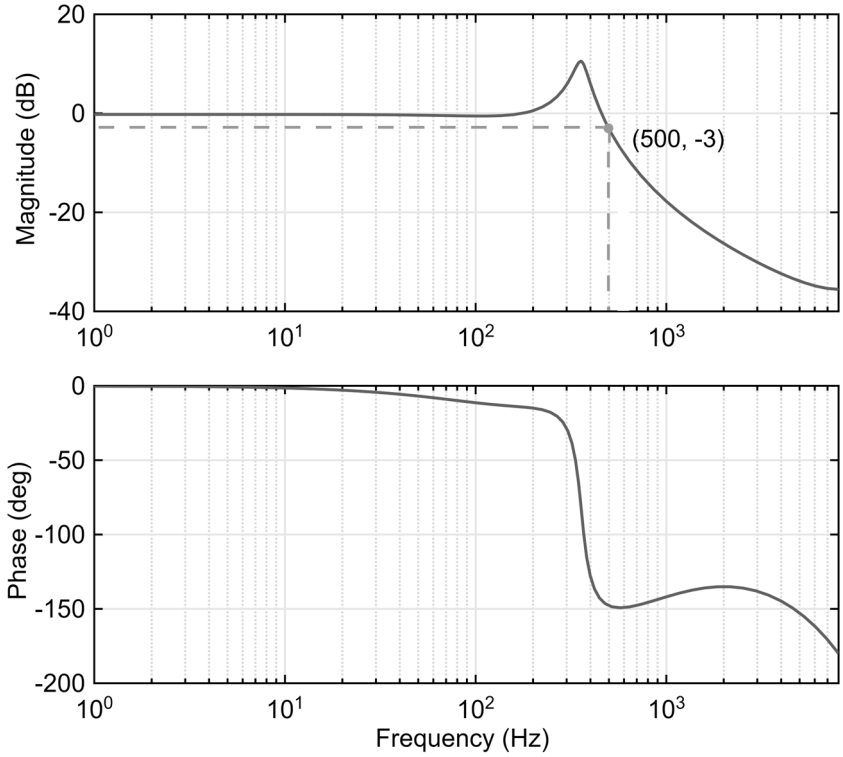


Figure 14. Bode diagram of the FTS system with the hybrid control algorithm.

4. Application in FTS Machining

4.1. Experiment Setup

To evaluate the practical machining flexibility and precision of the proposed algorithm, an ultrafine-grained aluminum sample was used for micro-pit FTS machining. As illustrated in Figure 15a, the designed microstructure array consists of spherical micro-pits. Each pit is a spherical cap defined by a large curvature radius (R_m) of 50 mm. With an opening diameter (D_m) of 1 mm, the depth of the micro-pits is calculated to be 2.5 μm according to Equation (21).

$$h_m = R_m - \sqrt{R_m^{\,2} - (\frac{D_m}{2})^2} \tag{21}$$

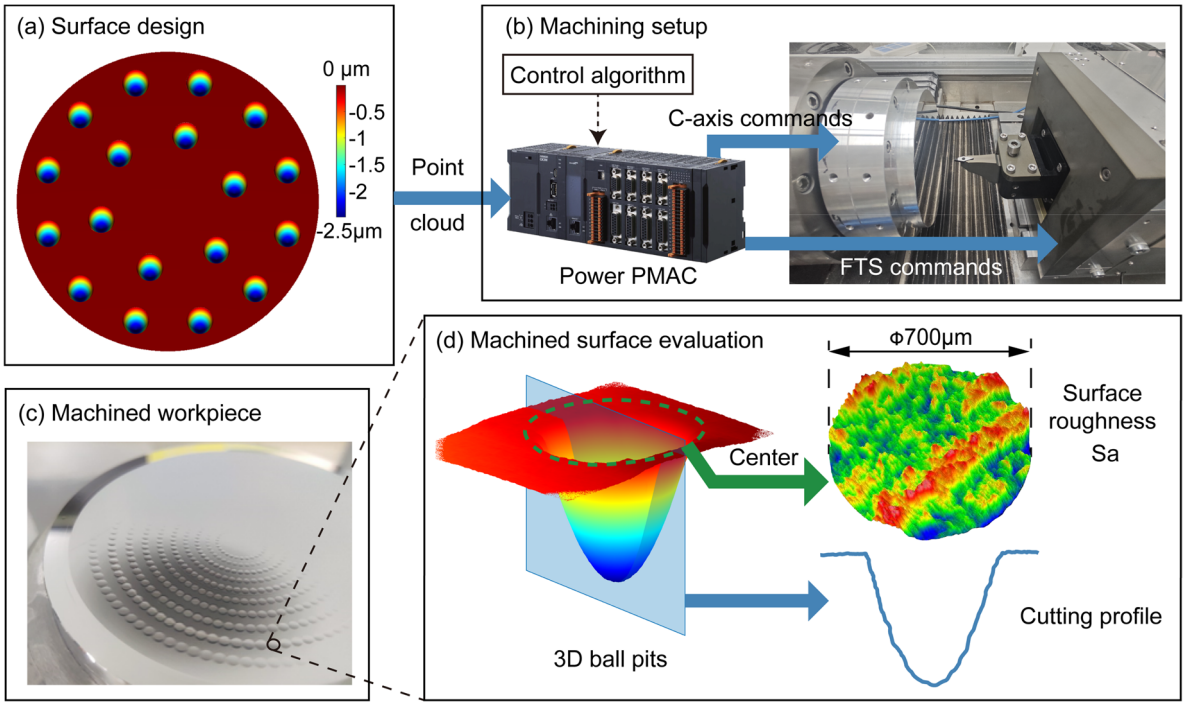


Figure 15. Schematic of (**a**) Surface design; (**b**) Machining setup; (**c**) Machined workpiece; (**d**) Machined surface evaluation.

The resulting workpiece surface shown in Figure 15c was characterized using white light interferometry (Zygo, Middlefield, CT, USA) to quantify key topographical metrics, as shown in Figure 15d. A single micro-pit was extracted from the machined array, with its cross-section analyzed to evaluate the cutting profile. The central evaluation region (diameter = 700 μm) was subsequently fitted with an ideal sphere, and the 3D surface morphology was constructed by subtracting the ideal spherical surface from the actual surface, enabling a quantitative evaluation of surface roughness.

4.2. Micro-Pit Array Machining

Before actual machining, a dry-run test was conducted to validate the flexibility of the proposed hybrid algorithm. Both the machine tool and FTS system followed the programmed trajectory under no-material-removal conditions. The following error was recorded as the difference between the command and the actual positions.

During the machining experiment, an ultrafine-grained aluminum workpiece was mounted on the machine spindle (C-axis) rotating at a constant speed as illustrated in Figure 15b. The measured surface roughness (arithmetic mean height S_a) under PID-FF and PID-FF-FSMC is visualized in Figure 16. A reduced surface roughness of 7.1 nm was achieved by the proposed hybrid algorithm, compared to 10.4 nm with PID-FF. Such an improvement in surface quality can be primarily attributed to the enhanced dynamics compensation and robustness to external perturbations, which considerably mitigate disturbance-induced errors and undesired vibrations during the high-frequency machining process.

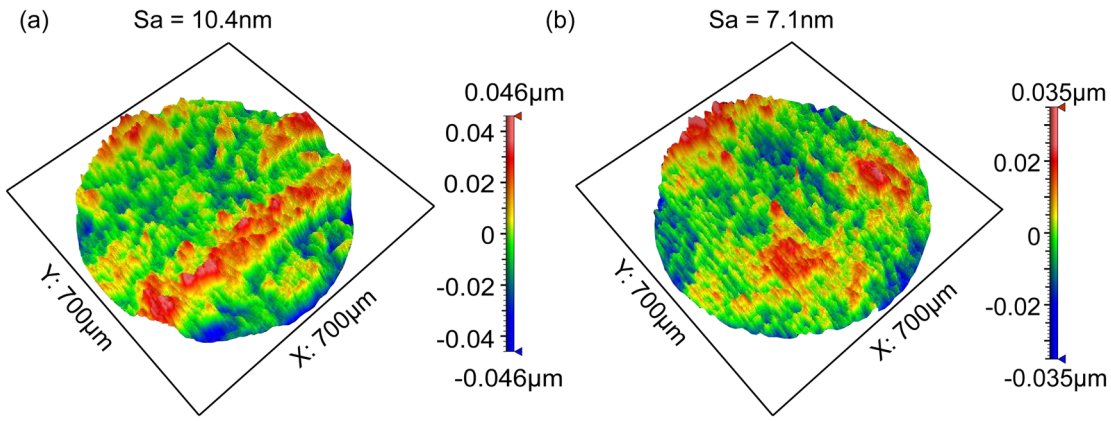


Figure 16. Surface morphology and roughness of the micro-pits under (**a**) PID-FF; (**b**) PID-FF-FSMC.

As illustrated in the cutting profile (Figure 17a), the hybrid control enables deeper material removal than the PID-FF, with fewer overshoot spikes shown in Figure 17b. Notably, while the FSMC markedly compensates for positive tracking errors, its corrective authority for negative errors is comparatively restrained. This directional asymmetry is attributed to the combined effects of controller saturation and frictional nonlinearity, which limit the corrective force available in the negative direction.

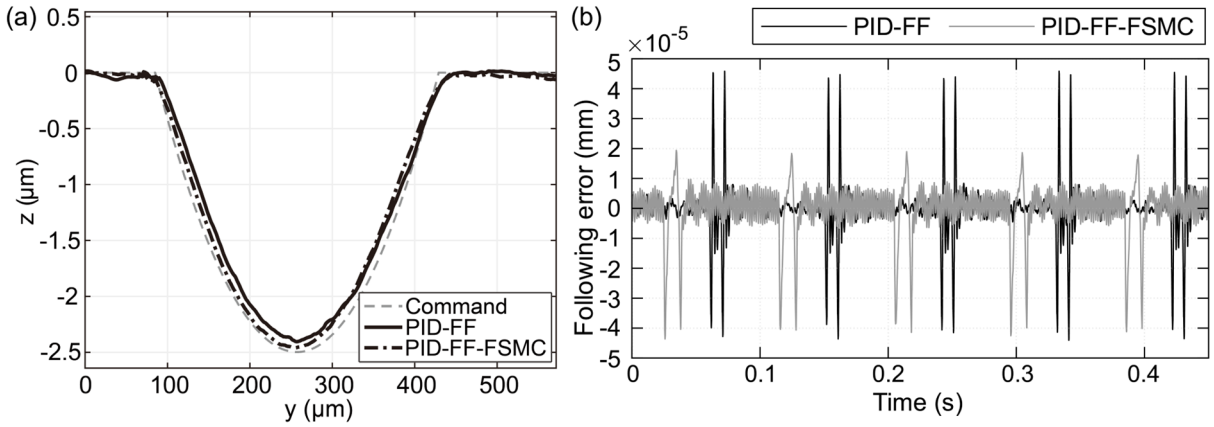


Figure 17. Tracking performance in micro-pit array machining. (**a**) Cutting profiles; (**b**) System following errors.

The *RMSE* and *SSE* results for the dry-run test and array machining experiment are summarized in Table 11. In the dry-run test, the PID-FF-FSMC exhibits significantly lower *RMSE* (0.3296%) and *SSE* (1.244%) than PID-FF (0.5497% and 1.5462%), confirming improved control precision and stability under no-load conditions. Moreover, the micro-pit array machining exhibits a noticeable reduction in tracking errors. The *RMSE* is decreased from 0.3441% (with PID-FF) to 0.3329% (with PID-FF-FSMC), and the hybrid algorithm reduced the maximum error by 3.37% compared to PID-FF. These measurement results support a machining benefit of the proposed hybrid control algorithm under the high-precision, high-frequency machining conditions.

Table 11. Summary of the following errors in FTS machining experiments.

Control Algorithms	Dry-Run Test		Machining Experiment	
	RMSE	***SSE***	***RMSE***	***SSE***
PID-FF	0.5497%	1.5462%	0.3441%	1.8556%
PID-FF-FSMC	0.3296%	1.244%	0.3329%	1.793%

5. Conclusions

In this work, a fuzzy sliding-mode-based hybrid control algorithm (PID-FF-FSMC) was developed for air-bearing machining systems. By addressing the trade-off among tracking accuracy, phase lag, and chattering that constrains conventional PID-FF and SMC-based schemes, the proposed framework advances air-bearing/FTS control under compressible air-film conditions. The main contributions are as follows.

(1) The proposed framework offers a unified hybrid control architecture that combines the complementary advantages of PID, feedforward (FF), and fuzzy sliding-mode control (FSMC). Its key advance is that fuzzy logic adaptively modulates the sliding-mode control action, suppressing chattering without sacrificing robustness. This directly addresses the long-standing conflict between disturbance rejection and chattering suppression in air-bearing/FTS control.

(2) The framework achieves enhanced disturbance rejection and wide-band tracking. Under simulated disturbance, the tracking error increased by 2.58 percentage points for PID-FF-SMC but only 0.57 percentage points for PID-FF-FSMC. Sinusoidal tracking tests at four frequencies further confirmed the advantage of the proposed controller, with the maximum tracking error reduced to 17.26% at 200 Hz and 0.43 μm amplitude. The FTS system achieved a measured closed-loop −3 dB bandwidth of approximately 500 Hz, a rise time of 1 ms, and an overshoot of 3.08%, while the air-bearing testbed achieved a rise time of 8 ms and an overshoot of 0.29%.

(3) The practical value of the framework was validated through FTS machining of ultrafine-grained aluminum. Compared with PID-FF, the hybrid controller reduced both the root mean square error (*RMSE*) and steady-state error (*SSE*). In micro-pit array machining, the arithmetic mean surface height (Sa) decreased from 10.4 nm with PID-FF to 7.1 nm with PID-FF-FSMC, a reduction of 31.73%, confirming improved tracking and surface quality.

Future work will focus on incorporating real-time adaptive tuning methods and developing advanced strategies for chatter suppression and nonlinear disturbance rejection, thereby extending the proposed framework to more complex machining applications.

Author Contributions

X.W.: Methodology, Investigation, Validation, Data curation, Writing—original draft preparation; Z.T.: Conceptualization, Supervision, Writing—review & editing, Funding acquisition; Z.G.: Methodology, Experimental guidance, Writing—review & editing; D.W.: Writing—review & editing. All authors have read and agreed to the published version of the manuscript.

Funding

This research was funded by the National Natural Science Foundation of China under Grant No. 23Z990302671.

Institutional Review Board Statement

Not applicable. This study involves numerical simulations and engineering experiments and does not involve human participants, human-derived materials, identifiable personal data, or animals.

Informed Consent Statement

Not applicable. This study does not involve human participants or identifiable personal data.

Data Availability Statement

Data will be made available on request.

Conflicts of Interest

The authors declare no conflict of interest.

Use of AI and AI-Assisted Technologies

No AI tools were utilized for this paper.

Nomenclature

Symbols	Parameter Name
A	Amplitude of sine signal
AD	Amplitude difference
A_1/A_2	Disturbance amplitudes
a	Actual acceleration
b	Weighting coefficient of fitness
c	Sliding surface coefficient
D_m	Opening diameter of spherical pits
e	Error
$\dot{e}$	Error derivative
F	Driving force
F_{RMS}	Root-mean-square thrust
F_{pk}	Peak thrust
f	Sine frequency
$f(S)$	Smooth approximation function
f_{sin}	Disturbance signal
g	Generation
gm	Transconductance
h_m	Maximum depth of spherical pits
I	Current
I_d	Command current
I_p	Proportional gain of PI controller
I_i	Integral gain of PI controller
k	Index of sample points
K_{aff}	Acceleration feedforward gain
K_e	Back EMF constant
K_f	Force constant
K_i	Integral gain
K_p	proportional gain

K_{vfb}	Velocity feedback gain
K_{vff}	Velocity feedforward gain
L	Inductance
m	Moving mass
N	Number of sample points
PD	Phase difference
R	Resistance
R_m	Radius of spherical pits
$RMSE$	Root-mean-square error
S	Sliding surface
S_a	Arithmetical mean height
S_{de}	Scaling factor of error derivative
S_e	Scaling factor of error
S_p	Scaling factor of stiffness coefficient
SSE	Steady-state error
S_c	Scaling factor of damping coefficient
T	Sine period
t	Time
$t_{d,p}$	Command displacement peak time
t_p	Actual displacement peak time
T_s	Sample interval
$u[k]_{\mathrm{FF}}$	Control law of FF
$u[k]_{\mathrm{FSMC}}$	Control law of FSMC
$u[k]_{\mathrm{PID}}$	Control law of PID
u_{model}	Input of state-space model
$u[k]$	Control law
v	Actual velocity
v_d	Command velocity
x	Actual displacement
x_d	Command displacement
$x(t)$	State vector of state-space model
$y(t)$	Output of state-space model
φ	Coefficient of tanh(•) function
$\hat{p}$	Stiff coefficient
$\hat{\varepsilon}$	Damping coefficient
ω	Angular velocity of sine signal

References

1. Rybus, T.; Seweryn, K. Planar air-bearing microgravity simulators: Review of applications, existing solutions and design parameters. *Acta Astronaut.* **2016**, *120*, 239–259. https://doi.org/10.1016/j.actaastro.2015.12.018.
2. Ise, T.; Nakatsuka, M.; Nagao, K.; et al. Externally pressurized gas journal bearing with slot restrictors arranged in the axial direction. *Precis. Eng.* **2017**, *50*, 286–292. https://doi.org/10.1016/j.precisioneng.2017.05.016.
3. Tonoy, A.A.R.; Ahmed, M.; Khan, M.R. Precision Mechanical Systems In Semiconductor Lithography Equipment Design And Development. *Am. J. Adv. Technol. Eng. Solut.* **2025**, *1*, 71–97. https://doi.org/10.63125/j6tn8727.
4. Sanz, C.; Gerard, R.; Morantz, P.; et al. Micro-scale finishing of the surface and form of a Ti-6Al-4V lightweight rotor obtained by laser powder bed fusion used for air bearing. *Addit. Manuf.* **2018**, *23*, 287–293. https://doi.org/10.1016/j.addma.2018.05.033.
5. Xiao, H.; Li, W.; Zhou, Z.; et al. Performance analysis of aerostatic journal micro-bearing and its application to high-speed precision micro-spindles. *Tribol. Int.* **2018**, *120*, 476–490. https://doi.org/10.1016/j.triboint.2018.01.002.
6. Huang, W.W.; Wang, X.; Meng, Y.; et al. Design, modeling and control of high-bandwidth nano-positioning stages for ultra-precise measurement and manufacturing: A survey. *Int. J. Extrem. Manuf.* **2024**, *6*, 062007. https://doi.org/10.1088/2631-7990/ad6ecc.
7. Tao, Y.; Chen, Y.L.; Hu, P.; et al. Development of a voice coil motor based fast tool servo with a function of self-sensing of cutting forces. *Precis. Eng.* **2020**, *65*, 130–137. https://doi.org/10.1016/j.precisioneng.2020.05.003.
8. Wen, Z.; Gu, H.; Shi, Z. Key Technologies and Design Methods of Ultra-Precision Aerostatic Bearings. *Lubricants* **2023**, *11*, 315. https://doi.org/10.3390/lubricants11080315.
9. Chen, X.; Luo, X.; Sun, Y.; et al. A novel bio-inspired compound restrictor for high-precision aerostatic bearings: Design and evaluation. *Precis. Eng.* **2026**, *97*, 348–366. https://doi.org/10.1016/j.precisioneng.2025.09.025.
10. Chen, X.; Luo, X.; Xie, W.; et al. Innovative Design of Aerostatic Bearings with Enhanced Dynamic Stability Inspired by the Laval Nozzle Principle. *Nanomanuf. Metrol.* **2026**, *9*, 2. https://doi.org/10.1007/s41871-025-00282-9.
11. Xu, X.; Liu, P.; Lu, S.; et al. Iterative Learning with Adaptive Sliding Mode Control for Trajectory Tracking of Fast Tool Servo Systems. *Appl. Sci.* **2024**, *14*, 3586. https://doi.org/10.3390/app14093586.

12. Mohindru, P. Review on PID, fuzzy and hybrid fuzzy PID controllers for controlling non-linear dynamic behaviour of chemical plants. *Artif. Intell. Rev.* **2024**, *57*, 97. https://doi.org/10.1007/s10462-024-10743-0.
13. Rakuff, S.; Cuttino, J.F. Design and testing of a long-range, precision fast tool servo system for diamond turning. *Precis. Eng.* **2009**, *33*, 18–25. https://doi.org/10.1016/j.precisioneng.2008.03.001.
14. Li, L.; Li, C.X.; Gu, G.; et al. Positive acceleration, velocity and position feedback based damping control approach for piezo-actuated nanopositioning stages. *Mechatronics* **2017**, *47*, 97–104. https://doi.org/10.1016/j.mechatronics.2017.09.003.
15. Huang, W.; Zhang, X.; Zhu, L. Repetitive-control-based Feedforward Compensation Method for Fast Tool Servo System. *J. Mech. Eng.* **2023**, *59*, 43–51. https://doi.org/10.3901/jme.2023.21.043.
16. Han, J. From PID to Active Disturbance Rejection Control. *IEEE Trans. Ind. Electron.* **2009**, *56*, 900–906. https://doi.org/10.1109/tie.2008.2011621.
17. Su, Z.G.; Sun, L.; Xue, W.; et al. A review on active disturbance rejection control of power generation systems: Fundamentals, tunings and practices. *Control Eng. Pract.* **2023**, *141*, 105716. https://doi.org/10.1016/j.conengprac.2023.105716.
18. Ji, Y.; Yang, Y.; Gao, Q.; et al. Q-learning Optimized Active Disturbance Rejection Control for Fast Tool Servo Systems. In Proceedings of the 2025 IEEE 26th China Conference on System Simulation Technology and Its Applications (CCSSTA), Shenzhen, China, 11–13 July 2025; pp. 182–187. https://doi.org/10.1109/ieeeconf65522.2025.11137051.
19. Xu, D.; Ding, B.; Jiang, B.; et al. Nonsingular Fast Terminal Sliding Mode Control for Permanent Magnet Linear Synchronous Motor via High-Order Super-Twisting Observer. *IEEE/ASME Trans. Mechatron.* **2022**, *27*, 1651–1659. https://doi.org/10.1109/tmech.2021.3086527.
20. Fu, D.; Zhao, X.; Zhu, J. A Novel Robust Super-Twisting Nonsingular Terminal Sliding Mode Controller for Permanent Magnet Linear Synchronous Motors. *IEEE Trans. Power Electron.* **2022**, *37*, 2936–2945. https://doi.org/10.1109/tpel.2021.3119029.
21. Mosquera, F.D.; Faedo, N.; Evangelista, C.A.; et al. Wave Energy Optimal Control Structure with Second-Order Sliding Mode Tracking: Hardware-in-the-Loop Assessment. *IEEE Trans. Sustain. Energy* **2024**, *15*, 1341–1350. https://doi.org/10.1109/tste.2023.3343995.
22. Li, L.; Zhou, W.; Bi, X.; et al. Speed Estimation of PMSM Based on a Super-Twisting Slide Mode Observer. *Machines* **2022**, *10*, 681. https://doi.org/10.3390/machines10080681.
23. Liu, Y.T. Recent Development of Piezoelectric Fast Tool Servo (FTS) for Precision Machining. *Int. J. Precis. Eng. Manuf.* **2024**, *25*, 851–874. https://doi.org/10.1007/s12541-023-00913-5.
24. Meng, Y.; Chen, Z.; Huang, W.W.; et al. An Enhanced Real-time Iterative Compensation Method for Fast Tool Servos with Resonance Suppression. *IEEE Trans. Ind. Electron.* **2024**, *71*, 6183–6192. https://doi.org/10.1109/tie.2023.3294632.
25. Zhou, R.; Wang, Z.; Lu, J.; et al. Ultraprecision multi-axis CARIC control strategy with application to a nano-accuracy air-bearing motion stage. *ISA Trans.* **2025**, *158*, 572–585. https://doi.org/10.1016/j.isatra.2025.01.020.
26. Abedali, G.H.; Bachache, H.K.; Mohammed, A.J.; et al. Designing Fuzzy Logic Control for the BLDC Motor Based on Airfoil Bearing. *Bilad Alrafidain J. Eng. Sci. Technol.* **2024**, *3*, 35–46. https://doi.org/10.56990/bajest/2024.030204.
27. Kumar, R.; Singh, U.P.; Bali, A.; et al. Hybrid Neural Network Control for Uncertain Nonlinear Discrete-Time Systems with Bounded Disturbance. *Wirel. Pers. Commun.* **2022**, *126*, 3475–3494. https://doi.org/10.1007/s11277-022-09875-9.
28. Sun, H.; Xing, N.; Zou, J.; et al. Neural Network-Based Switching Output Regulation Control for High-Speed Nano-Positioning Stages. *Engineering* **2026**, *57*, 227–235. https://doi.org/10.1016/j.eng.2025.07.023.
29. Chen, S.Y.; Chiang, H.H.; Liu, T.S.; et al. Precision Motion Control of Permanent Magnet Linear Synchronous Motors Using Adaptive Fuzzy Fractional-Order Sliding-Mode Control. *IEEE/ASME Trans. Mechatron.* **2019**, *24*, 741–752. https://doi.org/10.1109/tmech.2019.2892401.
30. Gong, Z.; Huo, D.; Niu, Z.; et al. Investigation of control algorithm for long-stroke fast tool servo system. *Precis. Eng.* **2022**, *75*, 12–23. https://doi.org/10.1016/j.precisioneng.2022.01.006.
31. Zhao, B.; Liu, Y.; Jia, D.; et al. Application of Fuzzy Sliding Mode Control in Voice Coil Motor Control System. *J. Phys. Conf. Ser.* **2022**, *2281*, 012009. https://doi.org/10.1088/1742-6596/2281/1/012009.
32. Huang, C.L.; Wang, T.; Li, M.; et al. Sliding Mode Control of Servo Feed System Based on Fuzzy Reaching Law. *Appl. Sci.* **2023**, *13*, 6086. https://doi.org/10.3390/app13106086.